Stretching and Breaking of Ultrathin MoS_2

Simone Bertolazzi,† Jacopo Brivio,† and Andras Kis*

Electrical Engineering Institute, Ecole Polytechnique Federale de Lausanne (EPFL), CH-1015 Lausanne, Switzerland. †These authors contributed equally to this work.

ABSTRACT

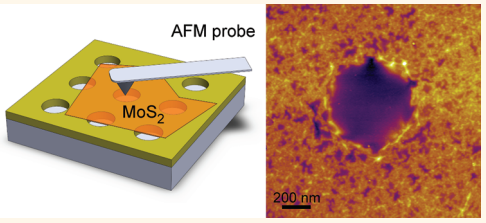

We report on measurements of the stiffness and breaking strength of monolayer MoS_2, a new semiconducting analogue of graphene. Single and bilayer MoS_2 is exfoliated from bulk and transferred to a substrate containing an array of microfabricated circular holes. The resulting suspended, free-standing membranes are deformed and eventually broken using an atomic force microscope. We find that the in-plane stiffness of monolayer MoS_2 is 180 $\pm$ 60 Nm^{-1}, corresponding to an effective Young's modulus of 270 $\pm$ 100 GPa, which is comparable to that of steel. Breaking occurs at an effective strain between 6 and 11% with the average breaking strength of 15 $\pm$ 3 Nm^{-1} (23 GPa). The strength of strongest monolayer membranes is 11% of its Young's modulus, corresponding to the upper theoretical limit which indicates that the material can be highly crystalline and almost defect-free. Our results show that monolayer MoS_2 could be suitable for a variety of applications such as reinforcing elements in composites and for fabrication of flexible electronic devices.

KEYWORDS: two-dimensional materials · dichalcogenides · MoS_2 · AFM · mechanical properties

Two-dimensional crystals, consisting of single or few atomic layers extracted from layered materials such as graphite or MoS_2,[1−3] are attracting a great deal of interest due to their promising potential for applications in nanotechnology. Graphene is the best known 2D material because of its high mobility, presence of massless Dirac fermions,[4,5] and a wealth of interesting physical phenomena such as the fractional quantum Hall effect.[6] Other 2D materials such as transition metal dichalcogenides or BN could have practical applications and fundamental properties complementary to those of graphene, although they are at this point much less explored.

Single-layer MoS_2 is a typical two-dimensional semiconductor from the class of layered transition metal dichalcogenides (TMD). Individual layers, 6.5 Å thick, can be extracted from bulk crystals using the micromechanical cleavage technique commonly associated with the production of graphene,[2,3] lithium-based intercalation,[7,8] or liquid phase exfoliation[9] and used as ready-made blocks for electronic device fabrication.[10] Bulk MoS_2 is an indirect gap semiconductor with a band gap of 1.2 eV (ref 11). Reducing the number of layers modifies the band structure and, as a consequence, monolayer MoS_2 becomes a direct gap semiconductor[12−15] with a band gap of 1.8 eV (ref 14) due to quantum confinement.[15] The presence of a band gap in monolayer MoS_2 makes it interesting for applications in nanoelectronics where it allows the fabrication of transistors with low power dissipation and current on/off ratios exceeding 10^8 at room temperature. Together with the possibility of large-scale liquid-based processing of MoS_2 and related 2D materials,[9] MoS_2 could also be very interesting for applications in flexible electronics where it would combine high performance with low cost. It is however not clear at this point if monolayer MoS_2 would be characterized by mechanical properties necessary for integration with stretchable polymer substrates in order to produce high-end bendable electronics.

Previous measurements on MoS_2 and WS_2 nanotubes,[16,17] which can be thought of as monolayers of MoS_2 and WS_2 wrapped up in the form of a cylinder, show superior mechanical properties with Young's modulus reaching 255 GPa and strength reaching 11% of its Young's modulus.[18,19] Subnanometer MoS_2 nanowires on the other hand have lower Young's modulus, 120 GPa.[20]

Here, we report on the measurement of the in-plane elastic modulus and breaking strength of single and bilayer MoS_2. MoS_2 consists of a stack of covalently bonded S−Mo−S layers weakly interacting with each other *via* van der Waals forces. The in-plane

* Address correspondence to andras.kis@epfl.ch.

Received for review August 19, 2011 and accepted November 9, 2011.

Published online 10.1021/nn203879f

crystal structure is determined by polar covalent bonds resulting from the overlap between the 4d and 3p electron orbitals of molybdenum and sulfur. The in-plane stiffness (E^{2D}) of an ideal defect-free single-layer MoS_2 is related to the effective spring constant of these molecular bonds. A defect-free material would have the upper theoretical limit of the breaking strength ($\sigma_{max}^{2D} \approx 10\%$ of the Young's modulus).[21] We use nanoindentation in an atomic force microscope in order to perform nanomechanical measurements on ultrathin MoS_2 suspended over circular holes in patterned substrates, using a technique previously used for measurements on multilayer[22,23] and single-layer graphene.[24] Mechanical properties of graphene have also been probed by performing uniaxial measurements.[25,26]

RESULTS AND DISCUSSION

Single- and few-layer MoS_2 was extracted from bulk crystals of naturally occurring MoS_2 using the micromechanical cleavage technique commonly employed for the production of graphene.[1] We found that direct exfoliation on patterned substrates yielded a relatively small number of samples, presumably because of reduced adhesion between the substrate and MoS_2. We therefore employed a transfer technique[27] to first exfoliate MoS_2 on polymer films and then transfer the resulting material onto prepatterned surfaces. MoS_2 is first deposited on Si substrates covered with 270 nm SiO_2 on top of which polyvinyl alcohol (PVA) and polymethyl methacrylate (PMMA) films have previously been spin-coated. We have reported elsewhere[28] that this SiO_2 thickness results in optimal visibility of monolayer MoS_2. Once an interesting flake with an optical contrast corresponding to a monolayer is located using an optical microscope, AFM is used to verify the thickness. The sample is then immersed in water to dissolve the PVA film and release the PMMA layer which ends up floating on the water surface. The film is moved onto a pierced glass slide and aligned to the new substrate with the help of a micromanipulator. The new substrate consisted of a 270 nm thick SiO_2 (ref 28) patterned with 550 nm diameter holes defined by e-beam lithography followed by dry etching. Finally, the sample is kept in vacuum at 400 °C for 4 h in order to release the polymer film without the use of solvents that could break MoS_2 during drying. In this way, we obtain a relatively high yield of intact MoS_2 membranes suspended over circular holes. Figure 1a shows a monolayer flake after the transfer on the new substrate, while Figure 1b shows a corresponding AFM image of the sample topography. Resulting suspended ultrathin layers of MoS_2 are tightly clamped to the edges of the holes, without visible wrinkles or discontinuities.

Mechanical properties of the membranes were probed with indentation experiments[29] using an AFM (Asylum Research Cypher) with a standard silicon

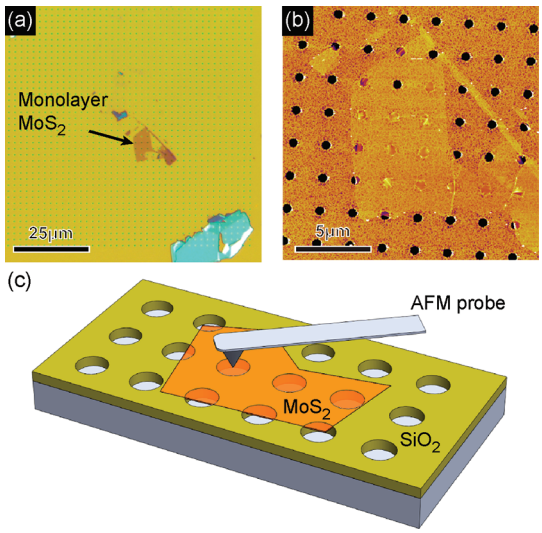

Figure 1. Sample preparation and the measurement method. (a) Optical image of a monolayer MoS_2 flake transferred onto the prepatterned SiO_2 substrate containing an array of circular holes 550 nm in diameter. (b) AFM image of the same single-layer MoS_2 as in part (a) shows that the monolayer is clean, free of wrinkles, and forms locally suspended membranes over multiple holes in the substrate. (c) Schematic depiction of the indentation experiment. During measurements, the AFM tip is placed above the center and slowly lowered while monitoring its deflection.

cantilever (Olympus AC240). Figure 1c shows the schematic depiction of the experiment. For each hole, an AFM topographical image of the suspended membrane was acquired in amplitude modulation mode and used to position the tip in the middle of the membrane; see Figure 2a.

Cantilever deflection is measured while the probe is moved in the vertical direction with a speed of 2 μm s^{-1}, resulting in controlled loading and unloading of the suspended MoS_2 membrane. Typical force *versus* piezo extension curves are shown on Figure 2d. Mechanical drift is minimized by means of a temperature controller integrated with the AFM system. Multiple curves with increasing indentation depths were acquired for each hole until mechanical failure was observed, as illustrated in Figure 2b. Mechanical failure typically occurs for vertical deflections <50 nm, well below the hole depth. No evidence of MoS_2 sheets sliding over the substrate was observed. The height profile in Figure 2c shows that the membrane adheres to the sidewalls of the hole over a distance on the order of 5 nm. This adhesion is due to van der Waals interaction and is presumably at the origin of the membrane pretensioning. Similar sidewall adhesion and pretension was reported in suspended graphene membranes.[24,30] SEM imaging was used to check tip quality, confirming that no damage occurred to the Si AFM tips during measurements. This observation is also supported by the fact that AFM image quality and measured results did not show any observable change during the experiment.

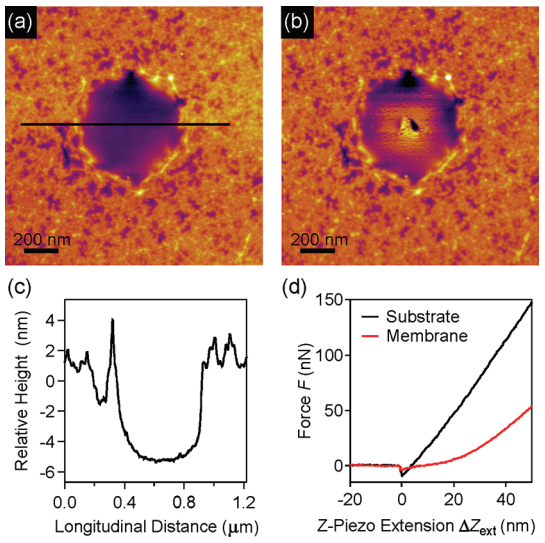

Figure 2. Suspended MoS_2 membranes and their mechanical failure. (a) AFM image of a monolayer MoS_2 flake suspended over a hole before the indentation experiment and (b) after it. A hole can be clearly seen in the center of the membrane at the location where the AFM tip punctured it. (c) Height profile of the section highlighted in (a) shows that the membrane adheres to the sidewalls over a vertical distance on the order of 5 nm, resulting in pretension between 0.02 and 0.1 Nm^{-1}. (d) Acquired force *versus* z-piezo extension curves for the suspended membrane and the substrate.

We performed experiments on a total of 9 monolayer (1 L) and 6 double-layer (2 L) MoS_2 membranes. A representative force *F versus* z-piezo extension (ΔZ_{ext}) curve for a monolayer membrane and the substrate is shown on Figure 2d. Loading and unloading curves in general overlap, indicating that no plastic deformation or membrane detachment occurs during the measurements and that the material can be considered as elastic.

The schematic diagram of the measurement geometry is given in Figure 3a. Because the measurement geometry (both tip and the sample) has circular symmetry and MoS_2 has six equivalent crystalline directions in terms of the stress-strain response, we model MoS_2 as an isotropic film characterized by Young's modulus E_Y, Poisson ratio ν and thickness h. Simulations on MoS_2 and measurements on WS_2 nanotubes[18,19] show that these materials related to monolayer MoS_2 are brittle and deform as materials with linear stress−strain relationship up to their failure. This is in stark contrast to carbon nanotubes or graphene where carbon atom chain formation and Stone-Wales transformations can lead to ductile behavior.[31] Such mechanisms are absent in MoS_2.[19] Because MoS_2 monolayers and nanotubes share the same type of chemical bonds, we also model MoS_2 as a linear elastic material.

The membrane is suspended over a circular hole with diameter $a = 2r = 550 \pm 10$ nm and deformed in the middle by an AFM tip with a radius $r_{tip} = 12 \pm 2$ nm. We suppose that the film is prestretched due to van der Waals adhesion between the film and the substrate leading to internal strain ε_0. Mechanical response of

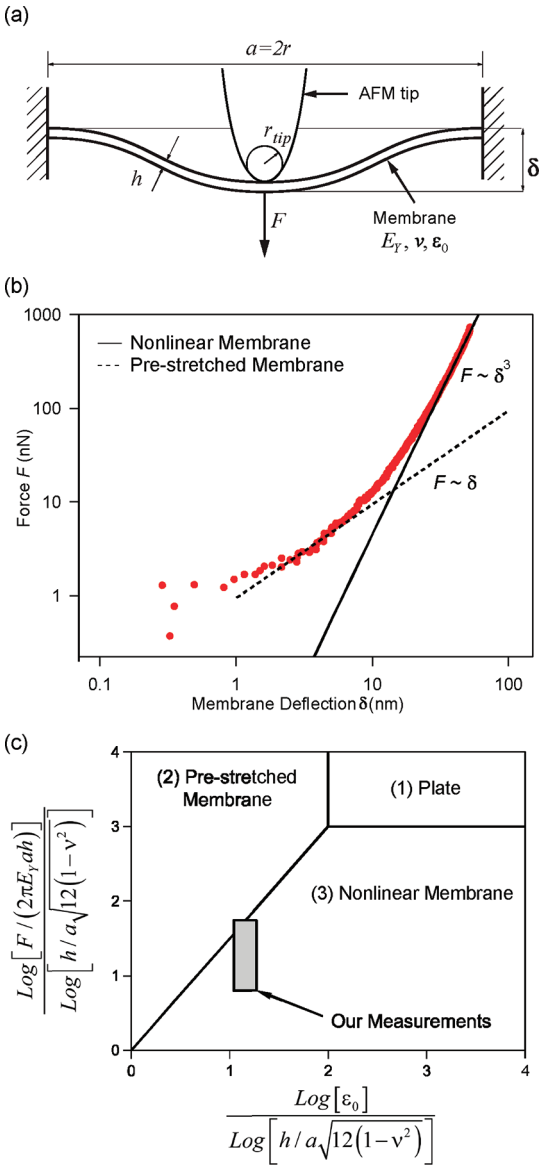

Figure 3. (a) Schematic diagram of the indentation test. A circular suspended membrane with Young's modulus E_Y, Poisson ratio ν, and prestrain ε_0 is elastically deformed in the middle by an AFM tip. The membrane is clamped at the edges and is loaded in the middle, resulting in membrane deflection δ. (b) Typical loading curve for a monolayer MoS_2 membrane. Small loads are characterized by a linear relationship between load F and deflection δ. For high loads, a cubic $F \sim \delta^3$ behavior dominates. (c) Parameter space according to Komaragiri *et al.*[32] delineating between different regimes of mechanical behavior for suspended circular membranes. The region in which our measurements are performed is shaded in gray.

such free-standing films can then fall into three distinct regimes, depending on the geometric factor h/a, applied load, and internal prestrain ε_0.[32] Linear plate bending and prestrained membrane deflection are characterized by linear force *versus* deflection behavior and are valid for small loads. Which one of these two governs the mechanical behavior depends on whether stiffness generated by prestrain is greater than the bending stiffness. The nonlinear membrane behavior

characterized by a cubic $F \sim \delta^3$ relationship dominates at large loads. In order to elucidate between these different deformation regimes, we plot a typical force–deflection curve in a logarithmic scale on Figure 3b. We can see that for small deflection and loading forces, limited by the resolution of our setup to ~1 nN, the curve follows a linear behavior (dashed line). For forces >10 nN, the curve starts to follow cubic behavior, typical of deformed membranes. We therefore fit the force–deflection data using a formula that captures both the linear behavior for small deformations and the cubic term for larger deformations:[32]

$$F = \sigma_0^{2D}\pi\delta + E^{2D}\frac{q^3\delta^3}{r^2} \quad (1)$$

where the cubic term containing the elastic modulus E^{2D} represents the modified form of the classical Schwerin solution for point loading of a circular membrane[33] valid for all values of the Poisson's ratio.[32] The term linear with deflection δ, where σ_0^{2D} is the prestress in the membrane, corresponds to the linear, prestretched membrane regime with an internal strain of ε_0.

Finite element simulations by Lee *et al.*[24] showed that this model can be applied to small and finite sized indenters as long as $r_{tip} \ll r$. We extract the tip radius r_{tip} ~ 12 nm from SEM images, resulting in $r_{tip}/r = 0.05$ in our case. The dimensionless constant q is related to the Poisson ratio ν as $q = 1/(1.05 - 0.15\nu - 0.16\nu^2) = 0.95$, where $\nu = 0.27$ is the Poisson ratio of bulk MoS_2.[34] The map of possible regimes of film response according to Komaragiri *et al.*[32] is presented on Figure 3c, together with the range of range of tests covered in this paper, confirming that most of the mechanical response that we record is expected to be in the region described by the cubic $F \sim \delta^3$ behavior.

Figure 4 shows representative experimental force–deflection curves acquired for mono- and bilayer MoS_2. From a least-squares fit of the experimental curves with the eq 1, we can extract the pretension σ_0^{2D} and the membrane elastic modulus E^{2D}. The fit agrees well with experimental data, validating our assumptions that led to the choice of eq 1 as the model. For a total of 9 monolayers (1 L), we obtain the average value for the elastic modulus E^{2D} of 180 ± 60 Nm^{-1} (Figure 5, left) and prestress σ_0^{2D} in the 0.02 to 0.1 Nm^{-1} range. Throughout the paper, the experimental uncertainty for the measured values of the elastic modulus and the breaking strength corresponds to the standard deviation of experimental values. Assuming an effective monolayer thickness of 0.65 nm, we obtain for the Young's modulus E_{Young} = 270 ± 100 GPa, close to the Young's modulus of MoS_2 nanotubes (230 GPa, ref 18), bulk MoS_2 (238 GPa, ref 34), or steel (210 GPa, ref 35). The elastic modulus of bilayer MoS_2 is 260 ± 70 Nm^{-1}, which corresponds to a lower Young's modulus of 200 ± 60 GPa, possibly due to defects or interlayer sliding.

During nanomechanical measurements, suspended membranes are deformed up to their mechanical failure, denoted by the symbol × in Figure 4, typically occurring for fracture forces of $F_{max} \approx$ 200 nN and

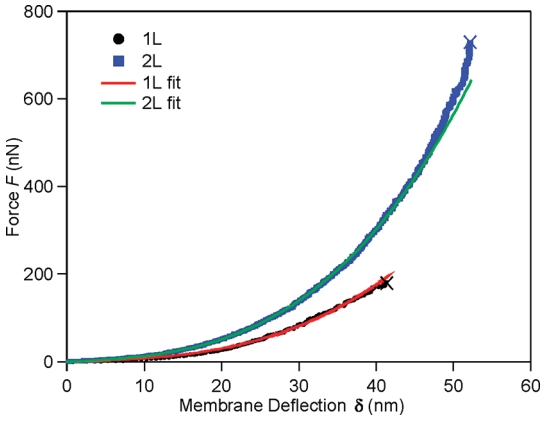

Figure 4. Examples of loading curves for single and bilayer MoS_2 and the least-squares fit of the experimental indentation curves to the eq 1. The fitting allows us to extract the pretension of the membrane σ_0^{2D} and its Young modulus E^{2D}. Experimental and fitted curves show good agreement. Membranes are fractured at the point marked by the symbol ×.

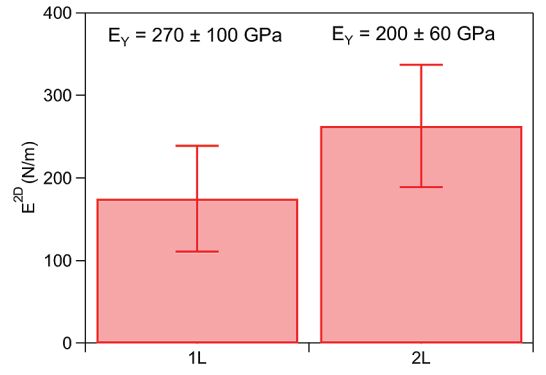

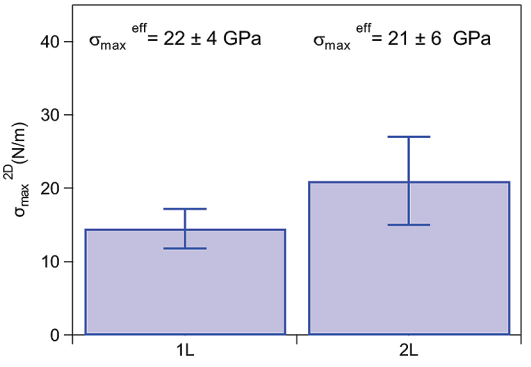

Figure 5. (Left) Young's modulus E^{2D} and (right) maximum breaking stress σ_{max}^{2D} at the central point of the film for 1 L and 2 L MoS_2 flakes extracted from the experimental data. The corresponding effective bulk modulus assuming a monolayer flake thickness of 6.5 Å is also shown for comparison with the bulk material.

TABLE 1. Comparison of Young's Moduli and Breaking Strengths for Several Engineering Materials, Including Monolayer MoS_2[19,24,34,35,39–43]

material	Young's modulus E_{Young} (GPa)	breaking strength σ_{max}^{eff} (GPa)	breaking strength/Young's modulus (%)
stainless steel ASTM-A514	205	0.9	0.4
molybdenum	329	0.5–1.2	0.15–0.36
polyimide	2.5	0.231	9
PDMS	0.3–0.87	2.24	2.5
Kevlar 49	112	3	2.6
monolayer MoS_2	270	16–30	6–11
bulk MoS_2	238		
WS_2 nanotubes	152	3.7–16.3	2.4–10
carbon nanotubes	1000	11–63	1.1–6.3
graphene	1000	130	13

deflections ≈50 nm. For such extreme deformation, in addition to large-scale deformation, the membrane is locally indented within a typical area extending $\sim 2r_{tip}$ distance from the center.[32] Here, the local curvature of the membrane is constrained by the tip diameter of the AFM probe, as long as the membrane is allowed to deform smoothly onto the indenter. Our experiment falls in the limit of small indenters characterized by $r_{tip}/r \ll 1$ ($r_{tip}/r = 0.05$ in our case) and large loads with respect to pretension, characterized by a factor $\kappa \ll 1$ defined as[36]

$$\kappa = \left(\frac{\sigma_0}{E_Y}\right)^{1/3}\left(\frac{2r_{tip}}{r}\right)^{2/3} \quad (2)$$

In our case, $\kappa < 0.02$. Here, we can extract the maximum stress at the central, protruding part of the film σ_{max}^{2D} using the expression for the indentation of a linearly elastic membrane by a spherical indenter in the limit of large load:[36]

$$\sigma_{max}^{2D} = \sqrt{\frac{F_{max}E^{2D}}{4\pi r_{tip}}} \quad (3)$$

The averages of maximum stress values for 1 L and 2 L-MoS_2 membranes are 15 ± 3 and 28 ± 8 Nm^{-1}, respectively (corresponding to 22 ± 4 GPa for a monolayer and 21 ± 6 GPa for a bilayer), as reported in Figure 4. On the average, these correspond to 8 and 10% of the Young's modulus for monolayer and bilayer MoS_2. The strength of individual MoS_2 monolayers is between 6 and 11% of their Young's modulus. These values are at the theoretical upper limit of a material's breaking strength and thus represent the intrinsic strength of interatomic bonds in MoS_2. This exceptionally high strength indicates that MoS_2 membranes are mostly defect-free. To put these high values of breaking strength and Young's modulus in perspective, we can compare them to several common engineering materials in Table 1. The strength of monolayer MoS_2 is exceeded only by carbon nanotubes and graphene. Even though MoS_2 has a smaller Young's modulus and strength than graphene, the absolute 2D elastic modulus E^{2D} and strength σ_{max}^{2D} of monolayer MoS_2 are smaller than those of graphene only by a factor of ∼2.

In order to investigate if MoS_2 could be suitable for integration with flexible materials, for example, in flexible electronic circuits, it is necessary to quantify the membrane strain at the breaking point, ε_{int}, and compare it to the breaking strain of standard flexible substrates. Assuming a linear relationship between stress and strain $\sigma = E\varepsilon$ leads to an internal stress at failure $\varepsilon_{int} \sim 0.06–0.11$.

In comparison, thin polymer films such as polyimide (PI) or polydimethylsiloxane (PDMS), commonly used as substrates for flexible electronics, break at a strain of ∼7% (ref 37), which is smaller than the aforementioned value extracted for single-layer MoS_2. This suggests that 2D MoS_2 can be readily integrated with PI or PDMS substrates for use in flexible electronics.

CONCLUSIONS

Our results show that monolayer MoS_2 is a flexible and strong material with a high Young's modulus, comparable to stainless steel. The measured strength of monolayer MoS_2 is close to the theoretical intrinsic strength of the Mo–S chemical bond, indicating that the monolayer is mostly free of defects and dislocations capable of reducing mechanical strength. As MoS_2 can be readily dispersed in a wide variety of solvents,[9] our finding indicates that MoS_2 could be interesting as a reinforcing element in composites. The presence of sulfur in MoS_2 could furthermore allow easy functionalization and efficient load transfer between MoS_2 and the composite matrix.

We also find that the exceptional mechanical properties of monolayer MoS_2 make it suitable for incorporation into flexible electronic devices where commonly used substrates such a PI would undergo mechanical failure at a smaller deformation than MoS_2.

MATERIALS AND METHODS

Single layers of MoS_2 are exfoliated from commercially available crystals of molybdenite (SPI Supplies Brand Moly Disulfide) using the scotch-tape micromechanical cleavage technique pioneered for the production of graphene.[1] Monolayer and few-layer MoS_2 was first deposited on a silicon substrate with 270 nm thick SiO_2 that has previously been coated with polyvinyl alcohol (Sigma-Aldrich) and polymethyl methacrylate (PMMA, Microchem Corp). The PMMA film is released by dissolving PVA in water and transferred on top of a prepatterned SiO_2 substrate. After transfer, PMMA is removed by heating the

sample in a vacuum furnace at 400 °C for 4 h. AFM imaging and indentation experiment was performed using the Asylum Research Cypher AFM equipped with the air temperature controller for minimizing drift and using Olympus AC240 silicon cantilevers. AFM probe spring constants were calibrated using the thermal method.[38]

Acknowledgment. Substrate fabrication was carried out in part in the EPFL Center for Micro/Nanotechnology (CMI). We thank Michael Brian Whitwick for help with SEM imaging of AFM tips. This work was financially supported the Swiss National Science Foundation (Grant No. 200021_132102) and the Swiss Nanoscience Institute (NCCR Nanoscience).

Supporting Information Available: SEM images of atomic force microscope probes. This material is available free of charge *via* the Internet at http://pubs.acs.org.

REFERENCES AND NOTES

1. Novoselov, K. S.; Geim, A. K.; Morozov, S. V.; Jiang, D.; Zhang, Y.; Dubonos, S. V.; Grigorieva, I. V.; Firsov, A. A. Electric Field Effect in Atomically Thin Carbon Films. *Science* **2004**, *306*, 666–669.
2. Frindt, R. F. Single Crystals of MoS_2 Several Molecular Layers Thick. *J. Appl. Phys.* **1966**, *37*, 1928–1929.
3. Novoselov, K. S.; Jiang, D.; Schedin, F.; Booth, T. J.; Khotkevich, V. V.; Morozov, S. V.; Geim, A. K. Two-Dimensional Atomic Crystals. *Proc. Natl. Acad. Sci. U.S.A.* **2005**, *102*, 10451–10453.
4. Novoselov, K. S.; Geim, A. K.; Morozov, S. V.; Jiang, D.; Katsnelson, M. I.; Grigorieva, I. V.; Dubonos, S. V.; Firsov, A. A. Two-Dimensional Gas of Massless Dirac Fermions in Graphene. *Nature* **2005**, *438*, 197–200.
5. Zhang, Y.; Tan, Y.-W.; Stormer, H. L.; Kim, P. Experimental Observation of the Quantum Hall Effect and Berry's Phase in Graphene. *Nature* **2005**, *438*, 201–204.
6. Du, X.; Skachko, I.; Duerr, F.; Luican, A.; Andrei, E. Y. Fractional Quantum Hall Effect and Insulating Phase of Dirac Electrons in Graphene. *Nature* **2009**, *462*, 192–195.
7. Joensen, P.; Frindt, R. F.; Morrison, S. R. Single-Layer MoS_2. *Mater. Res. Bull.* **1986**, *21*, 457–461.
8. Schumacher, A.; Scandella, L.; Kruse, N.; Prins, R. Single-Layer MoS_2 on Mica: Studies by Means of Scanning Force Microscopy. *Surf. Sci. Lett.* **1993**, *289*, L595–L598.
9. Coleman, J. N.; Lotya, M.; O'Neill, A.; Bergin, S. D.; King, P. J.; Khan, U.; Young, K.; Gaucher, A.; De, S.; Smith, R. J.; *et al.* Two-Dimensional Nanosheets Produced by Liquid Exfoliation of Layered Materials. *Science* **2011**, *331*, 568–571.
10. Radisavljevic, B.; Radenovic, A.; Brivio, J.; Giacometti, V.; Kis, A. Single-Layer MoS_2 Transistors. *Nat. Nanotechnol.* **2011**, *6*, 147–150.
11. Kam, K. K.; Parkinson, B. A. Detailed Photocurrent Spectroscopy of the Semiconducting Group Vib Transition Metal Dichalcogenides. *J. Phys. Chem.* **1982**, *86*, 463–467.
12. Lebegue, S.; Eriksson, O. Electronic Structure of Two-Dimensional Crystals from *Ab Initio* Theory. *Phys. Rev. B* **2009**, *79*, 115409.
13. Splendiani, A.; Sun, L.; Zhang, Y.; Li, T.; Kim, J.; Chim, C.-Y.; Galli, G.; Wang, F. Emerging Photoluminescence in Monolayer MoS_2. *Nano Lett.* **2010**, *10*, 1271–1275.
14. Mak, K. F.; Lee, C.; Hone, J.; Shan, J.; Heinz, T. F. Atomically Thin MoS_2: A New Direct-Gap Semiconductor. *Phys. Rev. Lett.* **2010**, *105*, 136805.
15. Kuc, A.; Zibouche, N.; Heine, T. Influence of Quantum Confinement on the Electronic Structure of the Transition Metal Sulfide TS_2. *Phys. Rev. B* **2011**, *83*, 245213.
16. Tenne, R.; Margulis, L.; Genut, M.; Hodes, G. Polyhedral and Cylindrical Structures of Tungsten Disulfide. *Nature* **1992**, *360*, 444–446.
17. Tenne, R.; Homyonfer, M.; Feldman, Y. Nanoparticles of Layered Compounds with Hollow Cage Structures (Inorganic Fullerene-like Structures). *Chem. Mater.* **1998**, *10*, 3225.
18. Kaplan-Ashiri, I.; Cohen, S. R.; Gartsman, K.; Rosentsveig, R.; Seifert, G.; Tenne, R. Mechanical Behavior of Individual WS_2 Nanotubes. *J. Mater. Res.* **2004**, *19*, 454–459.
19. Kaplan-Ashiri, I.; Cohen, S. R.; Gartsman, K.; Ivanovskaya, V.; Heine, T.; Seifert, G.; Wiesel, I.; Wagner, H. D.; Tenne, R. On the Mechanical Behavior of WS_2 Nanotubes under Axial Tension and Compression. *Proc. Natl. Acad. Sci. U.S.A.* **2006**, *103*, 523–528.
20. Kis, A.; Mihailovic, D.; Remskar, M.; Mrzel, A.; Jesih, A.; Piwonski, I.; Kulik, A. J.; Benoit, W.; Forró, L. Shear and Young's Moduli of MoS_2 Nanotube Ropes. *Adv. Mater.* **2003**, *15*, 733–736.
21. Griffith, A. The Phenomenon of Rupture and Flow in Solids. *Philos. Trans. R Soc.* **1920**, *221*, 163.
22. Frank, I. W.; Tanenbaum, D. M.; van der Zande, A. M.; McEuen, P. L. Mechanical Properties of Suspended Graphene Sheets. *J. Vac. Sci. Technol., B* **2007**, *25*, 2558–2561.
23. Poot, M.; van der Zant, H. S. J. Nanomechanical Properties of Few-Layer Graphene Membranes. *Appl. Phys. Lett.* **2008**, *92*, 063111.
24. Lee, C.; Wei, X.; Kysar, J. W.; Hone, J. Measurement of the Elastic Properties and Intrinsic Strength of Monolayer Graphene. *Science* **2008**, *321*, 385–388.
25. Mohiuddin, T. M. G.; Lombardo, A.; Nair, R. R.; Bonetti, A.; Savini, G.; Jalil, R.; Bonini, N.; Basko, D. M.; Galiotis, C.; Marzari, N.; *et al.* Uniaxial Strain in Graphene by Raman Spectroscopy: G Peak Splitting, Grüneisen Parameters, and Sample Orientation. *Phys. Rev. B* **2009**, *79*, 205433.
26. Tsoukleri, G.; Parthenios, J.; Papagelis, K.; Jalil, R.; Ferrari, A. C.; Geim, A. K.; Novoselov, K. S.; Galiotis, C. Subjecting a Graphene Monolayer to Tension and Compression. *Small* **2009**, *5*, 2397–2402.
27. Dean, C. R.; Young, A. F.; Cadden-Zimansky, P.; Wang, L.; Ren, H.; Watanabe, K.; Taniguchi, T.; Kim, P.; Hone, J.; Shepard, K. L. Multicomponent Fractional Quantum Hall Effect in Graphene. *Nat. Phys.* **2011**, *7*, 693–696.
28. Benameur, M. M.; Radisavljevic, B.; Heron, J. S.; Sahoo, S.; Berger, H.; Kis, A. Visibility of Dichalcogenide Nanolayers. *Nanotechnology* **2011**, *22*, 125706.
29. Weisenhorn, A. L.; Hansma, P. K.; Albrecht, T. R.; Quate, C. F. Forces in Atomic Force Microscopy in Air and Water. *Appl. Phys. Lett.* **1989**, *54*, 2651–2653.
30. Bunch, J. S.; Verbridge, S. S.; Alden, J. S.; van der Zande, A. M.; Parpia, J. M.; Craighead, H. G.; McEuen, P. L. Impermeable Atomic Membranes from Graphene Sheets. *Nano Lett.* **2008**, *8*, 2458–2462.
31. Nardelli, M. B.; Yakobson, B. I.; Bernholc, J. Brittle and Ductile Behavior in Carbon Nanotubes. *Phys. Rev. Lett.* **1998**, *81*, 4656–4659.
32. Komaragiri, U.; Begley, M. R.; Simmonds, J. G. The Mechanical Response of Freestanding Circular Elastic Films under Point and Pressure Loads. *J. Appl. Mech.* **2005**, *72*, 203–212.
33. Schwerin, E. Uber Spannungen Und Formänderungen Kreisringförmiger Membranen. *Z. Tech. Phys.* **1929**, *12*, 651–659.
34. Feldman, J. L. Elastic Constants of 2h-MoS_2 and 2h-$NbSe_2$ Extracted from Measured Dispersion Curves and Linear Compressibilities. *J. Phys. Chem. Solids* **1976**, *37*, 1141–1144.
35. Gere, J. M.; Timoshenko, S. P., *Mechanics of Materials*, 3rd ed.; PWS-Kent: Boston, MA, 1984; p 690.
36. Bhatia, N. M.; Nachbar, W. Finite Indentation of an Elastic Membrane by a Spherical Indenter. *Int. J. Non-Linear Mech.* **1968**, *3*, 307–324.
37. Kim, D.-H.; Ahn, J.-H.; Choi, W. M.; Kim, H.-S.; Kim, T.-H.; Song, J.; Huang, Y. Y.; Liu, Z.; Lu, C.; Rogers, J. A. Stretchable and Foldable Silicon Integrated Circuits. *Science* **2008**, *320*, 507–511.
38. Hutter, J. L.; Bechhoefer, J. Calibration of Atomic-Force Microscope Tips. *Rev. Sci. Instrum.* **1993**, *64*, 1868–1873.
39. Shinno, H.; Kitajima, M.; Okada, M. Thermal Stress Analysis of High Heat Flux Materials. *J. Nucl. Mater.* **1988**, *155−157*, 290–294.
40. Dupont Kapton Polyimide Film General Specifications, Bulletin Gs-96-7.

41. Armani, D.; Liu, C.; Aluru, N. In *Re-Configurable Fluid Circuits by Pdms Elastomer Micromachining*, Micro Electro Mechanical Systems, 1999. MEMS '99; 12th IEEE International Conference, 17−21 Jan, 1999; pp 222−227.
42. Kevlar Technical Guide.
43. Yu, M.-F.; Lourie, O.; Dyer, M. J.; Moloni, K.; Kelly, T. F.; Ruoff, R. S. Strength and Breaking Mechanism of Multiwalled Carbon Nanotubes under Tensile Load. *Science* **2000**, *287*, 637–640.